Reports

Morphology and Local Structure in Labyrinthine Stripe Domain Phase

M. SEUL,* L. R. MONAR, L. O'GORMAN, R. WOLFE

Analysis of globally disordered, nonequilibrium "labyrinthine" stripe-domain patterns in thin ferrimagnetic garnet films has revealed a well-defined local structure containing an oblong polygonal plaquette as the fundamental motif. Two types of labyrinths were found: one having topological defects, the other composed of a single, unbranched, meandering line. These patterns emerge when the labyrinthine state is approached either by heating at constant magnetic field or by demagnetizing from saturation at constant temperature. Size and aspect ratios of the oblong polygonal plaquettes prove to be independent of the choice of these two mutually orthogonal trajectories within the phase diagram, which is surprising in view of the different mechanisms and concomitant topological constraints governing the evolution of disorder. The significance of this unique local structure is discussed in the general context of defect-mediated melting of two-dimensional stripe phases.

UNIDIRECTIONALLY MODULATED ("lamellar") states occur in a wide variety of circumstances in condensed matter physics. In three dimensions, pertinent examples include the smectic phases of liquid crystals (*1*) and the analogous lamellar phases of surfactants and diblock copolymers (*2*). In two dimensions, "stripe" phases (*3*) are favored in systems with competing interactions, including thin uniaxial ferrimagnetic garnet films (*4*), layers of ferromagnetic colloids ("ferrofluids") (*5*), and amphiphilic ("Langmuir") monolayers confined to an air-water interface (*6*). Likewise, these phases are seen in monolayers of rare gas atomic and simple molecular adsorbates on crystalline substrates exhibiting transitions between commensurate and incommensurate phases (*7*) and in certain layered materials undergoing a charge density wave distortion (*8*). Even dissipative systems may display analogous structures, as in the case of the convective rolls arising from the Rayleigh-Bénard instability (*9*).

In all of these instances, the one-dimensional ordering is defined in terms of a modulation wave vector, $\mathbf{q}^*$. The corresponding length scale, $d \equiv 2\pi/|\mathbf{q}^*|$, is given in terms of characteristic molecular dimensions as in the case of liquid crystals and block copolymers, set by the balance of competing interactions (*4*) or determined by competing intrinsic periodicities (*3*); d may vary from tens of angstroms to millimeters (*10*). In general, $\mathbf{q}^*$ depends on temperature and chemical potential or an equivalent external field, and as these experimental variables are tuned, lamellar order eventually gives way to globally disordered states: in fact, "labyrinthine" patterns of the type of interest here have long been known in several of the systems mentioned above (*4, 5, 10, 11, 12*).

We present results of an examination of the morphology and local structure of such labyrinthine stripe patterns. This examination was performed by application of extensive digital line-pattern analysis to images recorded via polarization microscopy from ferrimagnetic garnet films. The composition of the films was $(YGdTm)_3(FeGa)_5O_{12}$, and they were grown epitaxially on gadolinium gallium garnet (GGG) substrates of (111) orientation to a thickness of approximately 13 μm. The direct-space analysis reveals the existence of a well-defined motif defining the local structure of these nonequilibrium states. That is, although the labyrinthine patterns generally do not represent the state of globally minimal free energy, they nevertheless exhibit a morphology that is characteristic of the final disordered state: the morphology is formed regardless of the choice of the specific trajectory in the magnetic field–temperature (H,T)-phase plane along which this state is approached. Labyrinthine patterns may thus be regarded as emerging from the minimization of a free-energy functional in the presence of well-defined constraints, imposed by the topology of the evolving pattern of nonintersecting lines.

To demonstrate the existence of this uniquely defined local structure of globally disordered stripe phases, we have examined the labyrinthine patterns generated from the initial states depicted in Fig. 1. These initial configurations represent distinct prototypes: one (Fig. 1A) is a well-ordered lamellar phase that is, in fact, the state of globally minimal free energy along the zero-field axis of the (H,T)-phase diagram (*4*); the other (Fig. 1B) is one of many possible configurations of a meandering stripe, emerging from a single site discernible in the figure.

The evolution of a labyrinthine pattern from the perfectly ordered lamellar phase of Fig. 1A, obtained from the paramagnetic phase by cooling in zero (perpendicular) magnetic field (*13*), involves a sequence of transverse instabilities similar to those displayed by smectic liquid crystals under elastic stress (*1, 14, 15*), and ends with the

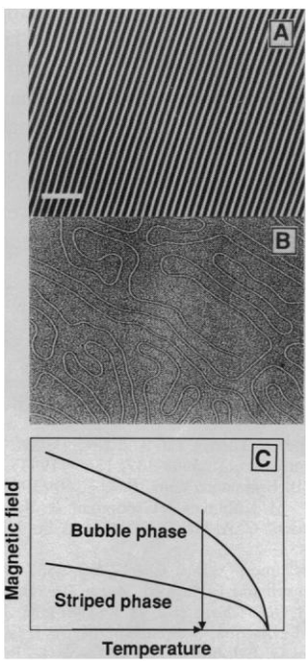

Fig. 1. Distinct types of magnetic stripe domain patterns rendered visible by Faraday effect and polarization microscopy. (**A**) Lamellar phase at $T \simeq 80°C$ ($\sim 0.76T_c$) and $H = 0$ Oe, generated by cooling at $H = 0$ Oe from the paramagnetic phase in the presence of a weak (~1/2 0 Oe) intraplanar field. The scale bar marks 200 μm; the characteristic stripe-stripe spacing, D^*, is 35.5 μm. (**B**) Meandering single stripe at $T \simeq 160°C$ ($\sim 0.93T_c$) and $H \simeq 70$ Oe, generated by demagnetizing at constant temperature from a state of complete magnetization. (**C**) Sketch of mean field (H,T)-phase diagram for the dipolar Ising ferromagnet exhibiting unidirectional "stripe" and triangular "bubble" phases (*4*). Horizontal and vertical arrows indicate the trajectories followed to obtain the labyrinth patterns of Fig. 2.

AT&T Bell Laboratories, Murray Hill, NJ 07974.

*To whom correspondence should be addressed.

formation and subsequent unbinding of disclination dipoles (*11, 15*). A detailed analysis of these instabilities will be presented elsewhere (*13*); the final labyrinthine pattern is of interest here.

Figure 2 shows the output of an algorithm designed to evaluate the medial axis transform ("skeleton") (*16*) of the "bright" component of a given pattern and to identify its topological defects (*17*): it is apparent that the pattern in Fig. 2A contains a random set of disclination charges of opposite sign (*18, 19*). As we show elsewhere, this configuration represents the result of an unbinding transition of initially paired disclination charges which remain topologically connected but move to otherwise uncorrelated positions (*13*). Starting with the meandering line in Fig. 1B, obtained by demagnetization from saturation at a temperature of 160°C ($\cong 0.93T_c$; critical T, $T_c \cong 192$°C), further reduction of the applied magnetic field to zero at this (constant) temperature produces the labyrinth, whose medial axis transform is depicted in Fig. 2B. In contrast to the previous case, topological defects are absent, on a scale of millimeters, from the pattern of the original "minority" (or "invading") phase, shown "bright" in Fig. 1B.

We may thus distinguish two types of labyrinths on the basis of topological point defects: we find in the first case a distribution of defects that is symmetric with respect to exchanging pattern components (see also Fig. 3A), while in the second case this symmetry is broken, leading to a completely asymmetric distribution: all defects are found in the "majority" component, shown "dark" in Fig. 1B. The first class of labyrinths containing disclinations in both components assumes the topology of a binary tree: it is referred to as "branched" below. The second class, here termed "banded," features a distinct component free of defects. Remarkably, the total density of disclinations is similar for both classes of patterns.

Azimuthally averaged Patterson or pair correlation functions were calculated for both types of labyrinths and for the lamellar ground state, all at $H = 0$ Oe and $T = 160$°C (Fig. 4). Two features are noteworthy. First, all three patterns are characterized by the same modulation wavenumber, that is, a specific value of $\mathbf{q}^* = \mathbf{q}^*(H,T)$: in fact, the realization of this uniquely determined value governs the pattern evolution from the initial state. Second, correlations in the labyrinth patterns in Fig. 4, A and C, vanish over a characteristic decay length of approximately 6 to 8 modulation periods, so stripe-stripe positional correlations are limited to that range.

Direct-space analysis of the labyrinth patterns accounts for the decay of the correlation functions in Fig. 4 by revealing the existence of a fundamental motif common to both types of labyrinths, namely, an oblong polygonal cluster of parallel line segments (*12, 20*). Application of low-pass and dilation filters (*20*) to the original pattern renders visible such segment clusters, prominent in the representation of the "branched" labyrinth in Fig. 3A. Line-pattern analysis yields a quantitative decomposition of the pattern into a set of clusters (Fig. 3B). To perform the analysis (*20*), one first processes a given pattern to approximate its medial axis transform by a set of linear segments, adjusting segment lengths in the fit (*21, 22*). A histogram of the size distribution of linear segments so obtained (Fig. 5A) reveals the presence of a preferred segment length, $\xi_\perp$, identical for both patterns, which may be regarded as the equivalent of a "persistence" length (*23*). The resulting set of linear segments is next subjected to a statistical analysis in which pairs of segments are compared with respect to three geometrical quantities measuring parallelism, mutual overlap, and adjacency (*17, 20*) and are sorted into groups, or segment clusters, according to a set of preselected threshold parameters. Finally, the convex hull of each cluster is constructed from the polygon defined by the ordered sequence of its segment endpoints (Fig. 3B) (*24*).

The segment clusters so generated are seen to yield a faithful representation of the local pattern structure. The equivalent of a nematic director (*1*), marking the average normal direction of segments in a group, may be assigned to each cluster (Fig. 3B). The corresponding order parameter, $S \equiv \langle 2\cos^2\phi - 1\rangle$, $0 \leq S \leq 1$, provides an average measure of alignment of individual directors in a preferred direction, with ϕ denoting the angular misorientation for a given director (*1*). Typical S values between 0.1 and 0.2 for the type of pattern analyzed here indicate the absence of a globally preferred direction, thereby implying complete azimuthal averaging of director orientations.

Statistical analysis of the longitudinal size,

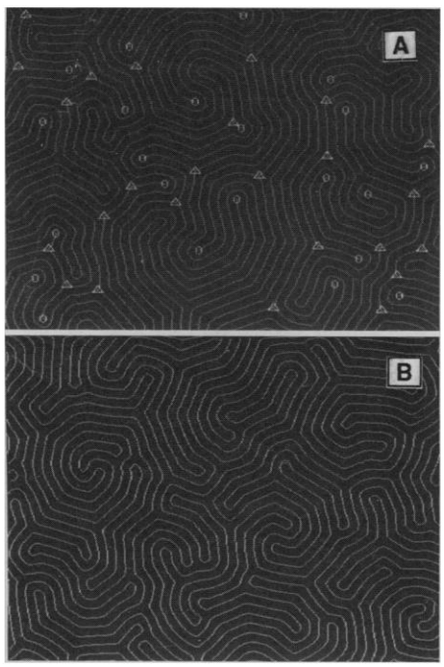

Fig. 2. Medial axial transform ("skeleton") of the "bright" component in labyrinth patterns of "branched" (**A**) and "banded" (**B**) types, generated, respectively, from the lamellar initial configuration of Fig. 1A by heating to ~160°C ($\sim 0.93T_c$) at $H = 0$ Oe and from the meandering stripe configuration of Fig. 1B by demagnetizing to $H = 0$ Oe at ~160°C, yielding zero net magnetization. (A) Disclination defects in the pattern of +1/2 (endpoints, ○) and −1/2 (branch points, △) charges impart the topology of a binary tree on this branched configuration (*13*). (B) The minority component of the banded labyrinth contains no topological defects. The width of the field measures 570 μm.

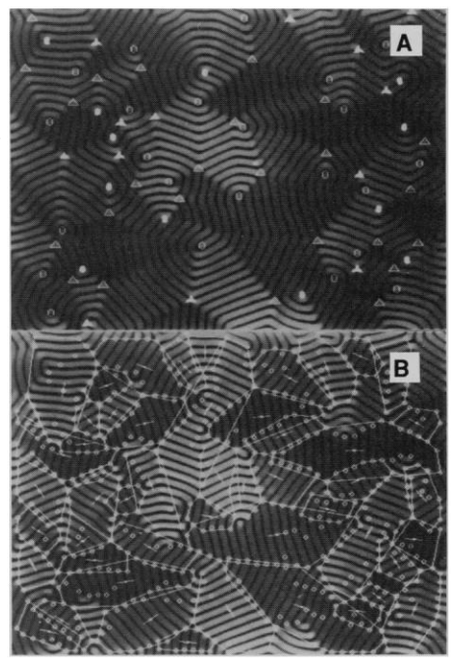

Fig. 3. Direct-space line-pattern analysis of branched labyrinth pattern. (**A**) Filtered version of the original pattern analyzed in Fig. 2A, processed to highlight oblong polygonal segment clusters. Topological defects in both bright and dark components of this "branched" labyrinth are identified as end points (○, ●) and branch points (△, ▲) of the pattern. (**B**) Each solid polygonal boundary represents the convex hull of a group of segments, computed from the segment endpoints (○). The line segment attached to each hull center marks the average normal of the segments grouped into the cluster and may be considered the equivalent of a nematic director. As discussed in the text, the pattern is globally isotropic: $S \simeq 0.2$. The width of the field is 570 μm.

$L \equiv (n - 1)d$, of segment clusters confirms that the correlation functions for both labyrinths given in Fig. 4, A and C, are in fact finite-size limited: the peak of the distribution of L for banded and branched labyrinths (Fig. 5C) coincides with the characteristic decay length of correlations. That is, longitudinal positional correlations, while expected to decay exponentially in two-dimensional (2-D) stripe phases (*19*), are here limited by the finite cluster size; effective elastic constants for stripe compression and bending, evaluated from "smectic" pattern instabilities (*13*), place typical positional correlation lengths in the range of 10 mm (*13, 15, 19*), a range far exceeding the typical peak values of L and reflecting the substantial effective stiffness of magnetic stripe phases (*15*).

The oblong clusters of Fig. 3 are reminiscent of those envisaged in the context of defect-mediated melting of a 2-D smectic phase in which the characteristic area and aspect ratio, $e \equiv L/W$, of a cluster are set by the density, n_D, of unpaired (free) dislocations. Specifically, scaling relations $A \approx \xi_D^2$, $L \approx \xi_D^{4/3}$, and $W \approx \xi_D^{2/3}$ are predicted, respectively, for area, length, and width of the clusters, where $\xi_D \simeq n_D^{-1/2}$ (*19*). The analysis of many labyrinth patterns (*20*) does indeed reveal that, in accordance with the cited scaling predictions, statistical fluctuations of cluster dimensions are correlated and may be described by $L \approx W^2$ for the range of typical cluster sizes encountered in our patterns. In fact, the inspection of "branched" labyrinths such as the one in Fig. 3A leads us to suggest that the density of disclinations plays a role analogous to n_D. That is, the geometrical dimensions of segment clusters are determined by the creation of disclinations at a characteristic density.

Thus, our picture of the formation of nonequilibrium labyrinth phases involves ideas germane to those advanced in the context of defect-mediated melting. While leading to exponentially decaying positional correlations, a finite density of free dislocations would leave orientational correlations intact; as a result, clusters would in that situation be expected to form a 2-D nematic phase characterized by a preferred direction of alignment of segment and algebraically decaying orientational correlations (*19*). In contrast, the segment clusters in our nonequilibrium labyrinthine patterns exhibit an isotropic distribution of orientations as we have stated in connection with Fig. 3. Topological constraints are seen to play a dominant role, generally preventing access to the state of globally minimal free energy. These constraints may be relaxed by breaking and reconnecting lines, thereby enabling the local reorientation of segment clusters. Such fluctuations, while not observed in the magnetic films investigated here, do occur in certain Langmuir films currently under study.

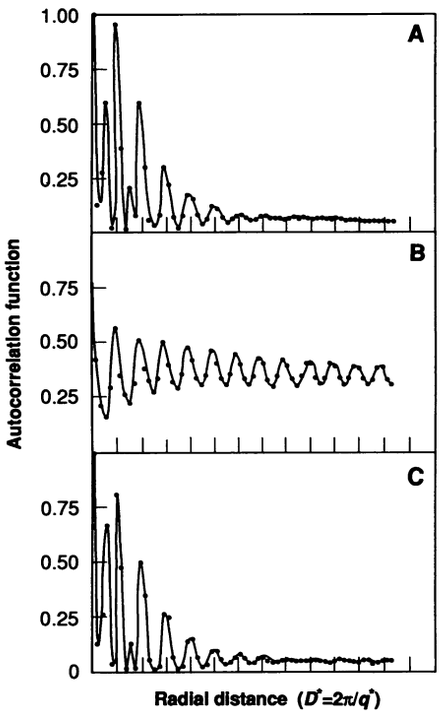

Fig. 4. Azimuthally averaged Patterson (pair correlation) functions, computed from (**A**) a branched labyrinth (see Fig. 2A), (**B**) a lamellar reference pattern, and (**C**) a banded labyrinth (see Fig. 2B) by successive 2*d* Fourier transformations and subsequent angular integration. All patterns were recorded at $T \simeq 160$°C and $H = 0$ Oe; the modulation period, d, is 11 μm.

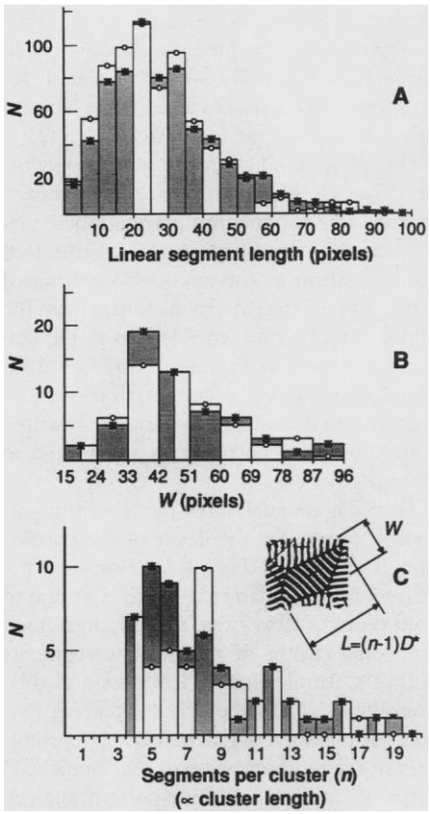

Fig. 5. Statistical analysis of oblong clusters in the "branched" (*) and "banded" (○) labyrinth patterns of Fig. 2. (**A**) Distribution of segment lengths (100 pixels = 111 μm) obtained when approximating the labyrinth patterns by a set of linear segments [for details, see (*20*)]: we identify the mean with a "persistence" length ($\sim 3d$) essentially identical for both types of patterns (total number of segments: *, 700; ○, 722). (**B**) Shape of the distribution of maximal cluster widths, W (100 pixels = 111 μm), reflects the existence of such a persistence length (total number of clusters: *, 58; ○, 53). (**C**) The distribution of longitudinal cluster sizes, L, is given in units of the stripe-stripe spacing, $d \equiv 2\pi/q^*$ (~ 11 μm); the peaks in the two distributions which are close [for more detail, see (*20*)], each representing the finite size cutoff which governs the decay of the corresponding positional correlation function in Fig. 4.

REFERENCES AND NOTES

1. P. G. deGennes, *The Physics of Liquid Crystals* (Clarendon Press, Oxford, 1974).
2. F. S. Bates, J. H. Rosedale, G. H. Fredrickson, *J. Chem. Phys.* **92**, 6255 (1990).
3. M. E. Fisher and A. M. Szpilka, *Phys. Rev. B* **36**, 644 (1982).
4. T. Garel and S. Doniach, *ibid.* **26**, 325 (1982).
5. R. E. Rosensweig, *Ferrohydrodynamics* (Cambridge Univ. Press, Cambridge, 1982), chap. 7.
6. M. Seul and M. J. Sammon, *Phys. Rev. Lett.* **64**, 1903 (1990); M. Seul, *Physica A* **168**, 198 (1990).
7. P. Bak, *Rep. Prog. Phys.* **45**, 587 (1982).
8. C. H. Chen, J. M. Gibson, R. M. Fleming, *Phys. Rev. B* **26**, 184 (1982).
9. J. Swift and P. C. Hohenberg, *Phys. Rev. A* **15**, 319 (1977).
10. T. Witten, *Phys. Today* **43**, 21 (July 1990).
11. P. Molho *et al.*, *J. Appl. Phys.* **61**, 4188 (1987).
12. I. B. Puchalska, G. A. Jones, H. Joure, *J. Phys. D* **11**, L175 (1978); I. B. Puchalska, plate IV in J. F. Dillon, Jr., *ibid.* **50**, i (1979); R. D. Pierce, *J. Cryst. Growth* **27**, 299 (1974).
13. M. Seul and R. Wolfe, in preparation.
14. R. Ribotta and G. Durand, *J. Phys. (Paris)* **38**, 179 (1977).
15. D. Sornette, *ibid.* **48**, 151 (1987); *ibid.*, p. 1413.
16. R. C. Gonzalez and P. Wintz, Digital Image Processing (Addison-Wesley, Reading, MA, 1987).
17. H. V. Jagadish and L. O'Gorman, *IEEE Comput.* **22**, 33 (1989); L. O'Gorman and G. I. Weil, in *Proceedings of the 8th International Conference on Pattern Recognition*, Paris, 27 to 31 October 1986 (IEEE Computer Society, Washington, DC, 1986), pp. 254–258.
18. Disclinations are topological defects which may be assigned a charge by noting that the unsigned layer normal undergoes a rotation through $\pm\pi = \pm 1/2 \times 2\pi$ in one circuit around a ± disclination [see also (*1, 15, 19*)].
19. J. Toner and D. R. Nelson, *Phys. Rev. B* **23**, 316 (1981); D. R. Nelson and J. Toner, *ibid.* **24**, 363 (1981).
20. M. Seul, L. R. Monar, L. O'Gorman, in preparation.
21. K. Wall and P.-E. Danielsson, *Comput. Vis. Graph. Image Process.* **28**, 220 (1989).
22. M. Seul, M. J. Sammon, L. R. Monar, *Rev. Sci. Instrum.* **62**, 784 (1991).
23. P. G. deGennes and C. Taupin, *J. Phys. Chem.* **86**, 2294 (1982).
24. The convex hulls of adjacent segment clusters are generally found, as in Fig. 3B, to partially overlap; this is a consequence of the distortions of the defining polygon of segment endpoints ("○" in Fig. 3B). This overlap is ignored in the statistical analysis of the clusters' geometrical characteristics. For a detailed discussion, see (*20*).

3 July 1991; accepted 17 September 1991